

BOSTON UNIVERSITY  
GRADUATE SCHOOL OF ARTS AND SCIENCES

Dissertation

**Something Something Something**  
**bla bla for Super Kamioknade**

by

**CHRISTOPHER J. KACHULIS**

B.S., Yale University, 2011

Submitted in partial fulfillment of the  
requirements for the degree of  
Doctor of Philosophy

2018

Approved by

First Reader

---

Edward T. Kearns, Ph.D.  
Professor of Physics

Second Reader

---

Someone, Ph.D.  
Associate Professor of Physics

# Acknowledgements

**Something Something SK**

(Order No.                      )

**Christopher Kachulis**

Boston University Graduate School of Arts and Sciences, 2018

Major Professor: Edward T. Kearns, Professor of Physics

ABSTRACT

# Contents

Acknowledgements	iii
Abstract	iv
Table of Contents	v
List of Tables	vii
List of Figures	viii
List of Abbreviations	xii
<b>1 Introduction</b>	<b>1</b>
1.1 A Brief History of the Neutrino . . . . .	1
<b>2 Neutrino Theory</b>	<b>3</b>
<b>3 The Super-Kamiokande Detector</b>	<b>4</b>
3.1 Overview . . . . .	4
3.2 Cherenkov Radiation . . . . .	5
3.3 The Tank . . . . .	7
3.4 Photomultiplier Tubes . . . . .	7

3.5	Electronics and Data Acquisition . . . . .	7
3.6	Water System . . . . .	7
3.7	Detector Calibration . . . . .	7
<b>4</b>	<b>Boosted Dark Matter</b>	<b>8</b>
4.1	Introduction . . . . .	8
4.2	Galactic Halo Models . . . . .	9
4.3	Event Selection . . . . .	12
4.4	Signal MC . . . . .	12
4.5	Ring Counting . . . . .	15
4.6	Analysis . . . . .	19
4.6.1	Trials Factors . . . . .	21
4.6.2	Limits on a simple Model . . . . .	22
4.7	Background Estimation . . . . .	26
4.8	Results . . . . .	33
4.9	Conclusion . . . . .	34
	<b>Bibliography</b>	<b>40</b>
	<b>Curriculum Vitae</b>	<b>43</b>

# List of Tables

4.1	Halo parameters for NFW, Moore, and Kravtsov models. The scale radius $r_s$ is in units of [kpc] while the two densities $\rho_0$ and $\rho(R_{sc})$ are in units of [GeV/cm <sup>3</sup> ]. $R_{sc}$ is the solar circle radius, 8.5 kpc [1]. . . .	10
4.2	Number of events in SK4 data passing each cut for 3 energy ranges. .	13
4.3	Largest systematic uncertainty contributions for High Energy sample.	33
4.4	Background estimates for the three energy ranges for 8 cone sizes around the galactic center and a 5° cone around the sun. Uncertainties on the background estimates are the systematic uncertainties as discussed in the text. . . . .	36
4.5	Results for low energy events . . . . .	37
4.6	Results for medium energy events . . . . .	38
4.7	Results for high energy events . . . . .	38

# List of Figures

3.1	Constructive interference resulting in Cherenkov radiation. . . . .	6
4.1	Moore (dashed green), NFW (solid blue) and Kravstov (dotted red) dark matter halo models. 4.1(a) shows the dark matter density as a function of distance from the galactic center. 4.1(b) and 4.1(c) show the J factors for the product of annihilating and decaying dark matter as a function of angle from the galactic center. Note that the x-axis is logarithmic on the left and linear on the right of 4.1(b) and 4.1(c). . .	11
4.2	Angular resolution for events passing all selection and analysis cuts, from signal MC in 3 energy ranges. . . . .	15
4.3	Energy resolution for events passing all selection and analysis cuts, from signal MC in 3 energy ranges. . . . .	15
4.4	Efficiency of the selection and analysis cuts as a function of energy. Beginning with the FCFV reduction (dashed-dotted blue), the addition of the 1-ring (dashed green), e-like (dotted red) and finally 0 decay electrons and 0 tagged neutrons cuts to arrive at the final efficiency (solid cyan) are shown. Note that the efficiency of the 0 decay electrons cut is $> 99.99\%$ , so that the drop from the dotted red line to solid cyan line is due solely to the background rate of the neutron tagging algorithm.	16



4.5	Example of a phantom ring found by APFIT. This is a single electron at 28 GeV. APFIT correctly finds the ring corresponding to the electron, but also finds an additional phantom ring . . . . .	17
4.6	Effeciency of the selection and analysis cuts as a function of energy, with no ring counting adjustment. Color scheme is the same as in Figure 4.4. Note the sharp drop in the efficiency of the 1-ring cut (dashed green). . . . .	17
4.7	Test variable for merging rings in high energy events. If $\alpha > 0.6$ , the ring is merged into the most energetic ring. . . . .	18
4.8	Cone opening angle optimization for boosted dark matter from annihilation and decay. In both 4.8(a) and 4.8(b) the solid blue is the NFW halo model, dotted red is the Kravtsov halo model, and dashed green is the Moore halo model. Note since the scaling is arbitrary, the efficiencies have been scaled by different amounts for each model so that they can all be seen on the same plot. . . . .	20
4.9	Trials factor effect. The dashed blue (dotted green) line converts the significance of an excess without the trials factor included into the significance with the trials factor included for the low (medium) energy sample, based on Toy MC. As reference, the solid red line shows $y=x$ , the conversion for perfectly correlated measurements, and the dashed-dotted cyan line shows the conversion for 8 uncorrelated measurements. Note that the effect for the galactic center cones falls between the perfectly correlated and perfectly uncorrelated effects, as expected. . .	22
4.10	Fenyman diagrams of boosted dark matter creation by annihilation of dominant heavy dark matter particles, and scatter of electron by boosted dark matter through exchange of a dark photon. . . . .	23

4.11	Recoil electron spectrum for simple model. The blue is for $m_{\gamma'} = 10$ MeV, while the red is for $m_{\gamma'} = 50$ MeV. Both use values of $m_A = 20$ GeV and $m_B = 200$ MeV. . . . .	24
4.12	“Away From Source” (AFS) region shown in blue, and search cone shown in gray for a search cone of $25^\circ$ half-opening angle around the galactic center. The red diamond is at the location of the galactic center. The dotted black line represents the $80^\circ$ cone outside of which the AFS region is defined. For an event at the location of the yellow star, the weight for background estimation is the ratio of the gray arc to the blue arc. . . . .	27
4.13	Visualization of the event weighting for background estimation. An event found in the AFS region at the declination represented by the plane is weighted by the ratio of the gray arc to the blue arc. Figure 4.13(b) shows Figure 4.13(a) as seen from directly above. The Mathematica code used to create these images can be found in ?? . . .	28
4.14	The fraction of time spent with $5^\circ$ of the sun, as a function of cosine zenith and azimuth. . . . .	31
4.15	Verification of AFS method. The blue histogram shows the fractional difference between the AFS background estimate when applied to MC and the actual number of events in the search cone in MC. The green shows the AFS background estimate uncertainty when applied to data.	32

4.16	Neutron tagging cut systematic error estimation. 4.16(a) shows the fractional number of events passing the neutron tagging cut after passing all previous cuts for both Data and MC, along with logarithmic fits. The filled rectangles around the MC show statistical uncertainty in the MC. 4.16(b) shows the resulting systematic uncertainty, set to 5% below 7.6 GeV, and the difference in the two fits from 4.16(a) above 7.6 GeV. . . . .	34
4.17	Comparison of AFS background estimates to MC background estimates for Low Energy and Mid Energy samples. The two background estimation techniques agree to within systematic uncertainties, and the AFS technique has much smaller systematic uncertainties. . . . .	35
4.18	Signal event rate 90% C.I. upper limits for SubGeV (solid line), Mid Energy (dashed line), and High Energy (dotted line) samples. . . . .	35
4.19	Location of all events passing analysis cuts near the galactic center. The 8 grey circles show the 8 cones around the galactic center used in the analysis. . . . .	36
4.20	Location of all events passing analysis cuts. The grey shows a 40° cone around the galactic center, which is shown by the red diamond . . . .	37
4.21	Limits on simple model, for $m_{\gamma'} = 20$ MeV. The dark blue line is for the NFW halo, and the upper and lower limits of the band are for the Kravtsov and Moore models, respectively. . . . .	39

# List of Abbreviations

ADC ..... Analog to Digital Converter

# Chapter 1

## Introduction

### 1.1 A Brief History of the Neutrino

While neutrinos have been around for about 13.8 billion years [2, 3], and humans for a slightly shorter but still respectable about 200,000 years, humans have only been aware of the neutrino for the relatively short period of about 90 years. The existence neutrino was first proposed by Wolfgang Pauli in a letter to a meeting in Tübingen, Germany, in 1930, as a possible explanation for the observed continuous beta decay spectrum [4]. In this letter Pauli wrote

...there could exist in the nuclei electrically neutral particles that I wish to call neutrons, which have spin  $1/2$  and obey the exclusion principle, and additionally differ from light quanta in that they do not travel with the velocity of light. The mass of the neutron must be of the same order of magnitude as the electron mass and, in any case, not larger than 0.01 proton mass.—The continuous  $\beta$ -spectrum would then become understandable by the assumption that in  $\beta$  decay a neutron is emitted together with the electron, in such a way that the sum of the energies of neutron and

electron is constant. [4]

This first proposal was tentative, and it is interesting to note that Pauli first used the name "neutron," the particle we today know as the neutron having not yet been discovered. In 1932, the heavy neutron we know today was discovered by James Chadwick, and so the light neutral particle first proposed by Pauli was renamed the "neutrino" by Enrico Fermi. In 1934, Fermi published a quantitative theory of  $\beta$ -decay which included neutrinos as an assumed component [5], and predicted the continuous beta-decay spectrum.

Continued measurements of the beta-decay spectrum and observations of new meson decays using nuclear track emulsion strengthened the evidence in the existence of the neutrino. However, it was not until the early 1950's that the neutrino was explicitly observed. Fred Reines and Clyde Cowan placed a large liquid scintillator detector near a nuclear reactor in Hanford, Washington. They hoped to observe neutrinos produced by the reactor interacting with the protons of the liquid scintillator through inverse beta decay,  $p + \bar{\nu} \rightarrow n + e^+$ . They searched for events with a delayed coincidence between the scintillation light due to the positron and the  $\gamma$  produced by the capture of the neutron on Cadmium with which the liquid scintillator had been loaded. They noted a change in the measured event rate when the reactor was on versus when it was off, which agreed well with the predicted neutrino event rate [6]. They soon confirmed the result with an upgraded experiment as Savannah River [7, 8].

## Chapter 2

# Neutrino Theory

# Chapter 3

## The Super-Kamiokande Detector

The Super Kamiokande detector is a large water Cherenkov detector in the Gifu, Japan. In this chapter an overview of the detector apparatus, detection principle, and detector calibration techniques are presented. Detailed overviews of the detector and detector calibration techniques can also be found in [9] and [10].

### 3.1 Overview

The SK detector is a large water Cherenkov detector located in the Mozumi mine below Mt. Ikenoyama in Gifu, Japan, with a mean overburden of 1000 m of rock (2700 m water-equivalent.). It consists of a 50 kT cylindrical tank of water, which is divided into a 32 kT inner detector (ID) surrounded by an 18 kT outer detector (OD). The ID and the OD are optically separated by black Tyvek sheeting, and both instrumented with photomultiplier tubes (PMTs) to observe Cherenkov radiation. It's large fiducial volume and high quality reconstruction capabilities make it an extremely effective detector for nucleon decay searches and studies of neutrinos over a wide range of energies.



The detector’s data taking lifetime, which began with it’s commissioning April 1996, is divided into four phases. The first phase, known as “SK-I”, acquired 1489.2 livetime days of data, running from commissioning until July 2001, when the detector was shut down for maintenance and upgrades. During the refilling of the tank in November 2001, an accident destroyed over half of the ID PMTs. The remaining ID PMTs were fitted with protective cases to avoid a future accident and redistributed, and the second phase, known as “SK-II”, ran from October 2002 until October 2005 with only half the ID PMT coverage of SK-I, acquiring 798.6 livetime days of data. During the shutdown after SK-II, new ID PMTs were added, and data taking resumed in July 2006 with the ID PMT coverage back at SK-I levels. This third phase is known as “SK-III”, and acquired 518.1 livetime days of data, running until September 2008, when the experiment was briefly shutdown for an electronics upgrade. Upon restarting in September 2008 SK entered it’s fourth phase, known as “SK-IV”, which is ongoing as of the writing of this thesis, and which has acquired 2867.2 livetime days of data as of May 2017. In total, SK has recorded 5673.1 livetime days of data (as of May 2017) with just over half of that data coming during SK-IV.

## 3.2 Cherenkov Radiation

When a charged particle travels through a material at a speed faster than the phase velocity of light in the material, Cherenkov radiation is produced. Molecules excited by the particle release light, and when the particle is traveling faster than  $c/n$ , the light emitted from different points along the particles path interferes constructively to create Cherenkov radiation, as shown in Figure 3.1. The requirement for Cherenkov radiation is thus

$$\beta > \frac{1}{n}. \quad (3.1)$$

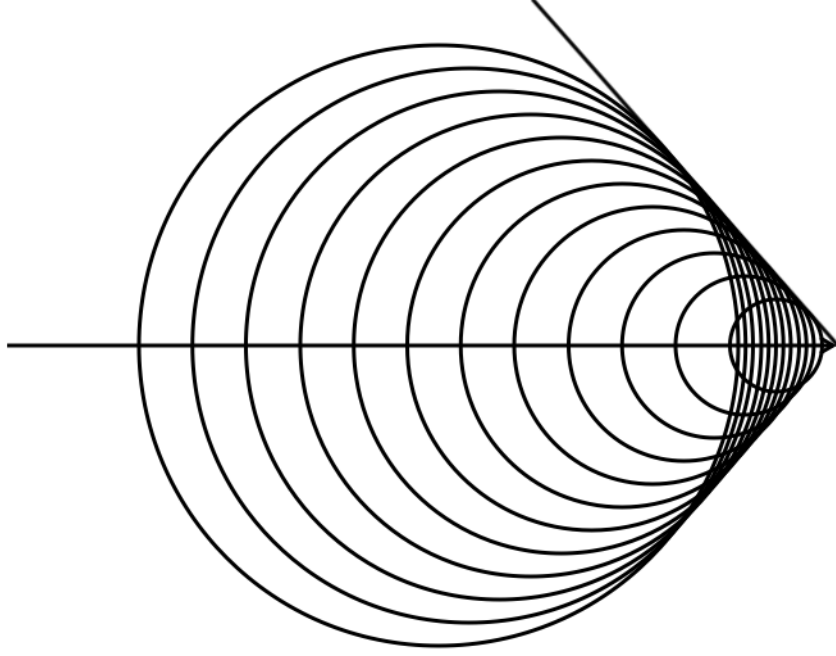


**Figure 3.1:** Constructive interference resulting in Cherenkov radiation.

The Cherenkov radiation is emitted from the path of the charged particle along a cone centered on the path of the charged particle with half opening angle  $\theta_C$  given by:

$$\cos \theta_C = \frac{1}{\beta n}. \quad (3.2)$$

A detailed derivation of these formula based on electrodynamics can be found in [11]. The index of refraction of water is 1.34, so for charged particles in water the cherenkov threshold corresponds to  $\beta > 0.75$ . This can be translated to a momentum threshold of  $p > 1.13m$ , which equates to a momentum threshold of 577 KeV/c for electrons, 119 MeV/c for muons, 157 MeV/c for charged pions, and 1.058 GeV/c for protons. The cherenkov angle for a highly relativistic charge particle in water ( $\gamma \gg 1$ ) of about  $42^\circ$ .

The emitted spectrum is described by the formula[12]:

$$\frac{d^2N}{d\lambda dx} = \frac{2\pi\alpha z^2}{\lambda^2} \left( 1 - \frac{1}{\beta^2 n^2(\lambda)} \right) \quad (3.3)$$

where  $\alpha$  is the fine structure constant,  $z$  is the charge of the particle (in units of electron charge),  $\lambda$  is the wavelength of the emitted light, and  $x$  is the distance traveled by the charged particle. It should be noted that while this formula allows for a wavelength dependent index of refraction, the index of refraction of water is quite stable over the range of wavelengths observed by PMTs.

### **3.3 The Tank**

The main component of the SK detector is a cylindrical stainless steel tank, with a diameter of 39 m and a height of 42 m. The tank is segmented into an

### **3.4 Photomultiplier Tubes**

### **3.5 Electronics and Data Acquisition**

### **3.6 Water System**

### **3.7 Detector Calibration**

# Chapter 4

## Boosted Dark Matter

### 4.1 Introduction

There is ample evidence for the existence of dark matter [13–16], and its abundance has been well measured to account for about 25% of the energy density of the universe [2, 3]. However, beyond its existence and abundance, little else is known about the properties of dark matter. A promising possible dark matter particle is the Weakly Interacting Dark Matter Particle (WIMP), but thus far attempts at its direct detection have left such a particle undiscovered [17–19]. Indirect detection of dark matter through the detection of its standard model annihilation products and detection of dark matter produced at particle accelerators have thus far similarly produced null results [20–25]. Boosted dark matter has been recently proposed in [26] and discussed as an alternative to the standard WIMP paradigm [27–31]. As opposed to WIMP models where the dominant dark matter particle couples directly to standard matter, in Boosted dark matter models the dominant dark matter particle instead couples to a lighter dark matter particle which in turn couples to standard matter. The lighter dark matter particle could be produced through annihilation,

semi-annihilation, or decay of the heavier dark matter particle, and if the mass difference between the dominant heavy dark matter and lighter sub-dominant dark matter is large enough these light dark matter particles will be relativistic. Reference [26] introduces an example model where the heavy dark matter particle annihilates into the lighter dark matter particle, which couples to standard model particles through the exchange of a dark photon. Such dark matter scenarios can be searched for by looking for the interaction of the boosted dark matter particle with standard matter. These interactions could be either with electrons, or nucleons. This technote reports a search for interactions of boosted dark matter particles with electrons in Super Kamiokande (SK), with the boosted dark matter originating either from the Galactic Center or the sun. In SK these interactions appear as elastically scattered electrons pointing back to either the Galactic Center or the sun. This search is performed on 2,628.1 days of SK-IV data, which corresponds to 161.9 kT-years.

## 4.2 Galactic Halo Models

Since the boosted dark matter being searched for comes from some interaction of the heavy non-interacting dark matter, its directional distribution around the galactic center is dependent on the density profile of the dark matter halo around the galactic center. A general form for the density profile (assumed to be spherically symmetric) from cold dark matter simulations is [1]

$$\rho(r) = \frac{\rho_0}{(r/r_s)^\gamma [1 + (r/r_s)^\alpha]^{(\beta - \gamma)/\alpha}} \quad (4.1)$$

Parameters of Equation 4.1 for the NFW [32], Moore [33], and Kravtsov [34] halo

models are shown in Table 4.1.

	$\alpha$	$\beta$	$\gamma$	$r_s$	$\rho_0$	$\rho(R_{sc})$
Moore	1.5	3	1.5	28	0.0527	0.27
NFW	1	3	1	20	0.259	0.3
Kravtsov	2	3	0.4	10	0.703	0.37

**Table 4.1:** Halo parameters for NFW, Moore, and Kravtsov models. The scale radius  $r_s$  is in units of [kpc] while the two densities  $\rho_0$  and  $\rho(R_{sc})$  are in units of [GeV/cm<sup>3</sup>].  $R_{sc}$  is the solar circle radius, 8.5 kpc [1].

The rate of boosted dark matter events coming from the annihilation or decay of dark matter from a particular direction in the sky is proportional to the so called “J-factor”, which is the line of sight integral of dark matter density for decay, or density squared for annihilation, and is a function of the angle between the event direction and the direction to the galactic center:

$$\mathcal{J}_{ann}(\theta_{GC}) = \frac{1}{R_N \rho_N^2} \int_0^{l_{\max}} \rho^2 \left( \sqrt{R_{sc}^2 - 2lR_{sc} \cos \theta_{GC} + l^2} \right) dl \quad (4.2)$$

$$\mathcal{J}_{decay}(\theta_{GC}) = \frac{1}{R_N \rho_N} \int_0^{l_{\max}} \rho \left( \sqrt{R_{sc}^2 - 2lR_{sc} \cos \theta_{GC} + l^2} \right) dl \quad (4.3)$$

where  $\theta_{GC}$  is the angle to the Galactic Center and  $R_{sc}$  is the solar circle radius (8.5 kpc). The upper limit of integration  $l_{\max}$  is defined by the adopted halo size  $R_{MW}$ :

$$l_{\max} = \sqrt{R_{MW}^2 - R_{sc}^2 \sin^2 \theta_{GC}} + R_{sc} \cos \theta_{GC}. \quad (4.4)$$

While the halo size  $R_{MW}$  appears to be an additional important parameter,  $\rho$  drops off sharply past 20-30 kpc, as shown in 4.1(a), so that the calculation of  $\mathcal{J}$  is insensitive to the chosen value of  $R_{MW}$  as long as it is above this range. The prefactors  $\frac{1}{R_N \rho_N^2}$  and  $\frac{1}{R_N \rho_N}$  in Equations 4.2 and 4.3 are arbitrary scaling factors used to make  $\mathcal{J}$

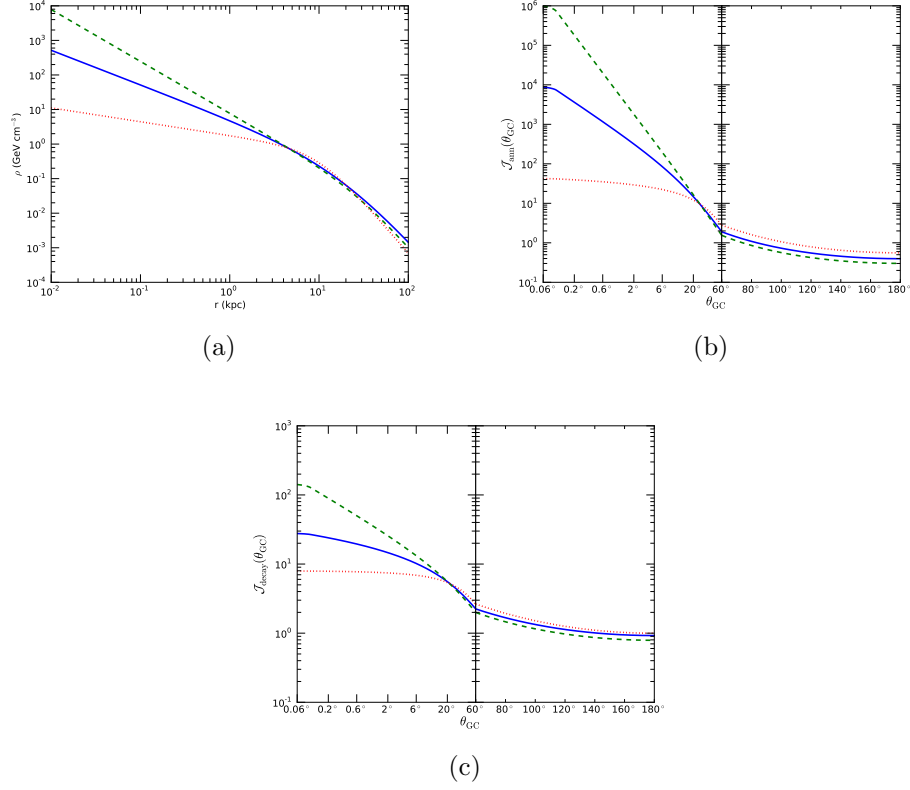


**Figure 4.1:** Moore (dashed green), NFW (solid blue) and Kravstov (dotted red) dark matter halo models. 4.1(a) shows the dark matter density as a function of distance from the galactic center. 4.1(b) and 4.1(c) show the J factors for the product of annihilating and decaying dark matter as a function of angle from the galactic center. Note that the x-axis is logarithmic on the left and linear on the right of 4.1(b) and 4.1(c).

dimensionless. Figure 4.1 shows the dark matter halo density J factors for the Moore, NFW, and Kravstov models. The J factors in 4.1(b) and 4.1(c) are calculated with  $R_{\text{MW}} = 40$  kpc and the standard scaling choice of  $R_N = R_{\text{sc}} = 8.5$  kpc,  $\rho_N = 0.3$   $\text{GeV}/\text{cm}^3$ . The J factor is taken to be flat at the innermost  $0.1^\circ$  to avoid divergence of  $\mathcal{J}$  due to cuspy profiles, which may be an artifact of simulation [1].

### 4.3 Event Selection

A cut based selection is used to select electron elastic-scatter-like events. The selection begins with the FCFV sample, which consists of all events which pass the Fully-Contained event reduction, plus four additional cuts:  $\text{wall} > 200$  cm, which defines the fiducial volume,  $\text{nhitac} < 16$ ,  $\text{evis} > 30$  MeV, and if the event is 1-ring like, the final cut  $\text{amome} > 100$  MeV. From this FCFV sample, 4 analysis cuts are applied:

1. 1-ring
2. e-like
3. 0 decay electrons
4. 0 tagged neutrons

The first two cuts search for the single relativistic scatter from an electron elastic scatter, while the final two cuts remove events with any indication of a nuclear interaction. The number of events found in all SK-IV after each cut is shown for three different energy ranges in 4.2 The neutron tagging cut plays an important role in background reduction, particularly in the high energy sample, as can be seen in Table 4.2. It's inclusion limits the current analysis to SK-IV only, since neutron tagging is not possible on SK-I-III data.

### 4.4 Signal MC

In order to study the efficiency of the event selection and the optimal opening angle for a Galactic center search, a signal monte carlo of 200,000 electromagnetic



	Evis<1.33 GeV	1.33 GeV<Evis<20 GeV	20 GeV< Evis
FCFV	15206	4908	97
and single ring	11367	2868	53
and e-like	5655	1514	53
and 0 decay-e	5176	1134	17
and 0 tagged neutrons	4132	683	4

**Table 4.2:** Number of events in SK4 data passing each cut for 3 energy ranges.

shower events was produced, with electron energies ranging from 30 MeV to 1 TeV. The MC was split into 4 energy ranges: 30 MeV-1 GeV, 1 GeV-10 GeV, 10 GeV-100 GeV, and 100 GeV to 1 TeV. Fifty thousand events were produced in each energy range, with a flat linear energy spectrum in each range. Event positions within the detector were randomly selected uniformly within a cylinder 1 meter inside the wall of the inner detector, in order to account for migration of events in the fiducial volume, which is 2 meters inside the wall of the inner detector.

The direction of the electromagnetic showers was chosen assuming the NFW annihilation model. For each event, a random direction in equatorial coordinates was chosen so that the probability of an event's source being placed at an angle  $\theta_{GC}$  from the galactic center is proportional to  $\mathcal{J}_{ann}(\theta_{GC}) \sin \theta_{GC}$ . The  $\sin \theta_{GC}$  factor is a geometrical affect. Note that we are simulating a case where the scattered electrons direction is exactly parallel to the direction of the boosted dark matter. While there would be expected to be some model dependent smearing of the boosted dark matter direction to the electron direction, the scattering is expected to be strongly peaked in the forward direction [26]. Thus, since it both has a minimal effect and is model dependent, the effect of this scattering directional smearing is ignored in the production of the signal MC. In order to transform from equatorial coordinates to the horizontal coordinates of the detector, a random time is chosen for each event. These times are randomly distributed at times during Super-K good data runs which are

used in the analysis. The time chosen for an event is then used to transform from equatorial to horizontal coordinates. While the simulation is created assuming the NFW annihilation model, other models can be studied by reweighting each event by the ratio of the new models J-factor to the NFW annihilation J-factor:

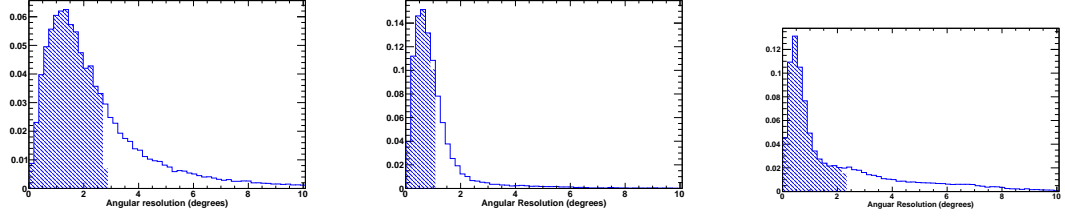
$$w_{\text{Model X}} = \frac{\mathcal{J}_{\text{Model X}}(\theta_{\text{GC}})}{\mathcal{J}_{\text{NFW ann}}(\theta_{\text{GC}})} \quad (4.5)$$

The Model dependent smearing mentioned above can similarly be added back into the simulation by event reweighting.

The signal MC was run through the most of the full SK MC production process: Simulation (SKDETSIM), FC reduction (FCCOMB), reconstruction (APFIT), and ntuple creation (FILLNT,ROOT2ZBS). The only portions of the full SK MC production process excluded were PC and UPMU reduction (since this is an FC only analysis), fitQun reconstruction (since this analysis uses only APFIT variables), and neutron tagging. Although neutron tagging is an extremely important part of this analysis, there are no simulated neutrons in the signal MC, so we can safely assume that the background rate of false positive neutron tags in the signal MC is the same as the background rate found in the atmospheric MC (1.8%).

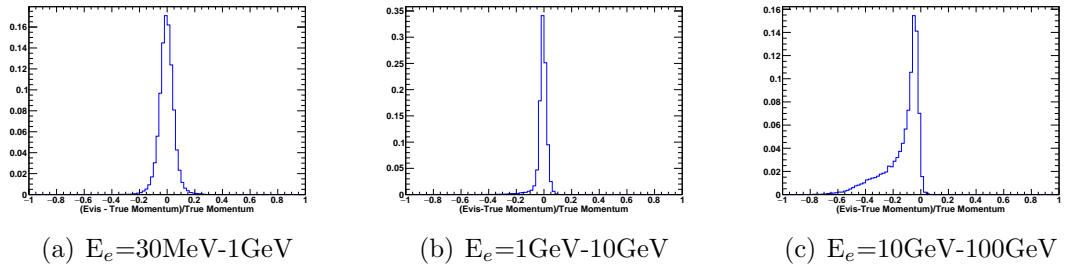
The angular and energy resolutions for events passing all selection and analysis cuts are shown in Figures 4.2 and 4.3. As can be seen in Figure 4.2, the angular resolution for these events is better than  $3^\circ$  for all energy ranges. The bias towards understating the energy in the high energy range (Figure 4.3(c)) and long tail on the negative side is due to the detector becoming saturated for very high energy events.

The efficiency of the selection and analysis cuts is shown in Figure 4.4. Efficiency is defined as the number of events passing a set of cuts divided by the number of events simulated in the fiducial volume. This is not exactly equivalent to the fraction



(a)  $E_e=30\text{MeV}-1\text{GeV}$ ,  $\sigma=2.8^\circ$  (b)  $E_e=1\text{GeV}-10\text{GeV}$ ,  $\sigma=1.1^\circ$  (c)  $E_e=10\text{GeV}-100\text{GeV}$ ,  $\sigma=2.3^\circ$

**Figure 4.2:** Angular resolution for events passing all selection and analysis cuts, from signal MC in 3 energy ranges.



(a)  $E_e=30\text{MeV}-1\text{GeV}$

(b)  $E_e=1\text{GeV}-10\text{GeV}$

(c)  $E_e=10\text{GeV}-100\text{GeV}$

**Figure 4.3:** Energy resolution for events passing all selection and analysis cuts, from signal MC in 3 energy ranges.

of events produced in the fiducial volume which pass all cuts, as some events will migrate into the fiducial volume to offset events migrating out of the fiducial volume. The total efficiency of the analysis turns on around 100 MeV and stays above 90% until around 5-10 GeV, and then remains above 80% until around 50 GeV. The main cause of the reduction of efficiency with energy is the loss of containment at high energies; many higher energy electromagnetic showers are able to penetrate from the FV into the OD, and so do not pass fully-contained cuts.

## 4.5 Ring Counting

The ring counting algorithms in APFIT have never been tuned for high energy events. As it turns out, APFIT finds phantom rings in many high energy electro-

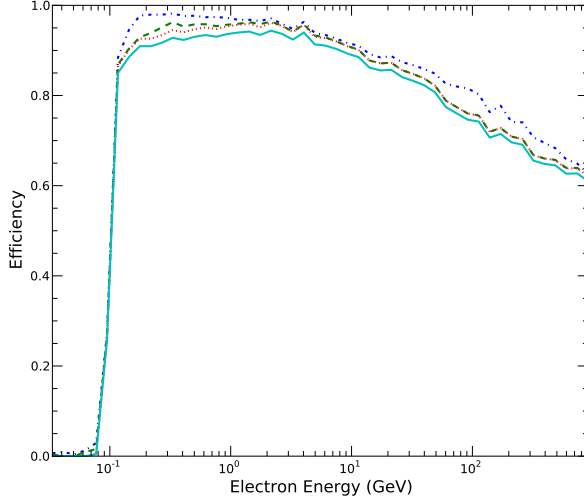


**Figure 4.4:** Efficiency of the selection and analysis cuts as a function of energy. Beginning with the FCFV reduction (dashed-dotted blue), the addition of the 1-ring (dashed green), e-like (dotted red) and finally 0 decay electrons and 0 tagged neutrons cuts to arrive at the final efficiency (solid cyan) are shown. Note that the efficiency of the 0 decay electrons cut is  $> 99.99\%$ , so that the drop from the dotted red line to solid cyan line is due solely to the background rate of the neutron tagging algorithm.

magnetic showers, as in Figure 4.5. Because of this, the efficiency of the 1-ring cut for this analysis drops off very sharply around 10 GeV if no adjustment is made, as shown in Figure 4.6.

These phantom rings are caused by fluctuations in the light patterns of high energy events. Because there is a large amount of light in a high energy event, these statistical fluctuations can trick APFIT into thinking it sees a low energy ring in addition. To fix this pathology, a test variable is constructed to merge rings which could reasonably be caused by statistical fluctuations:

$$\alpha_{i_{\text{ring}}}^2 = \frac{1}{N_{\text{PMT}, \theta < 70^\circ}} \sum_{j_{\text{PMT}, \theta < 70^\circ}} \frac{Q\text{Dev}_{i_{\text{ring}}, j_{\text{PMT}}}^2}{Q\text{Dev}_{i_{\text{MER}}, j_{\text{PMT}}}} \quad (4.6)$$

where  $N_{\text{PMT}, \theta < 70^\circ}$  is the number of PMT's within  $70^\circ$  of the direction of the ring,  $i_{\text{MER}}$

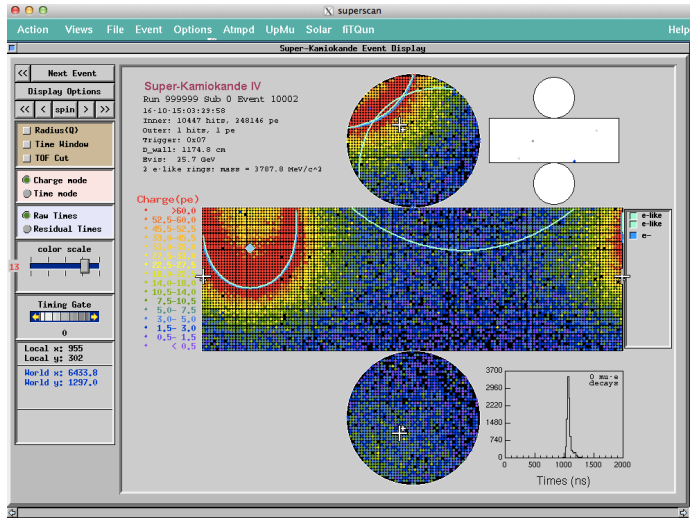


**Figure 4.5:** Example of a phantom ring found by APFIT. This is a single electron at 28 GeV. APFIT correctly finds the ring corresponding to the electron, but also finds an additional phantom ring

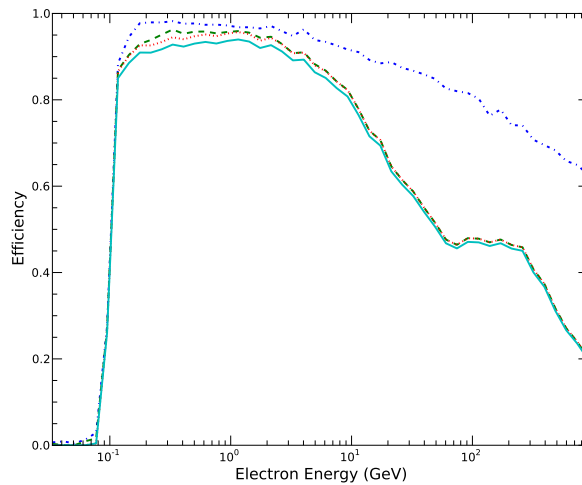


**Figure 4.6:** Efficiency of the selection and analysis cuts as a function of energy, with no ring counting adjustment. Color scheme is the same as in Figure 4.4. Note the sharp drop in the efficiency of the 1-ring cut (dashed green).

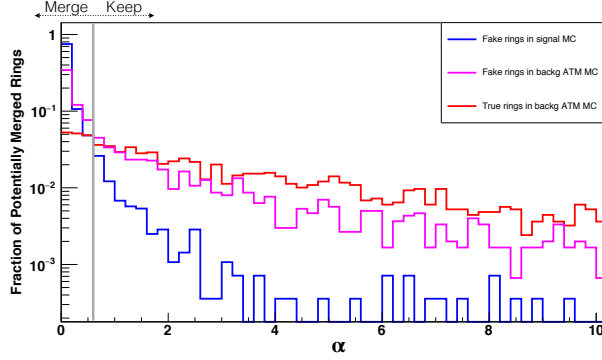


**Figure 4.7:** Test variable for merging rings in high energy events. If  $\alpha > 0.6$ , the ring is merged into the most energetic ring.

is the index of the most energetic ring, and  $QDev_{i,j}$  is the devided charge of the  $j^{\text{th}}$  PMT assigned to the  $i^{\text{th}}$  ring, defined as:

$$QDev_{i,j} = Q_j^{\text{measured}} \frac{Q_{i,j}^{\text{expected}}}{\sum_k Q_{k,j}^{\text{expected}}} \quad (4.7)$$

where  $Q_{i,j}^{\text{expected}}$  is the charge expected in the  $j^{\text{th}}$  PMT due to the  $i^{\text{th}}$  ring and  $Q_j^{\text{measured}}$  is the charge measured in the  $j^{\text{th}}$  PMT.  $QDev_{i,j}$  is stored in the common block array APPEDEV in APFIT. In order to fill APPEDEV with usable values, `sprngsep(2,1,1,3)` is run. For rings which are not the most energetic ring,  $\alpha$  is calculated, and the ring is merged into the most energetic ring if  $\alpha < 0.6$ . Figure 4.7 shows the distribution of values of  $\alpha$  for real and fake rings in the signal electromagnetic shower and background atmospheric neutrino MC. Since, the 1-ring cut efficiency is only problematic at high energies, this merging technique is only applied to events with  $E_{\text{vis}} > 1.33$  GeV. With merging, the efficiency improves from that seen in Figure 4.6 to that seen in Figure 4.4, with minimal increase of the atmospheric background.

## 4.6 Analysis

The analysis technique is very simple; Count the number of events in a cone drawn around the potential source, and determine if this number is consistent with the expected background of atmospheric neutrinos. In order to choose the optimal opening angle for a galactic center search, a figure of merit is defined as  $\text{Efficiency}/\sqrt{\text{Bckg}}$  for different cone half opening angles, using the signal MC described in Section 4.4 to compute the Efficiency for each cone and the official SK atmospheric MC for the number of events expected in the cone. These figures of merit for cone half opening angles up to  $40^\circ$  are shown in Figure 4.8. In these figures of merit we care only about the shape not the magnitudes of the  $\text{Efficiency}/\sqrt{\text{Bckg}}$ , so the values for different models have been scaled by different amounts so that they can be seen together on the same plot. As can be seen, the optimal angle ranges from  $< 5^\circ$  for NFW dark matter annihilation to  $> 40^\circ$  for Kravtsov dark matter decay. Because of this, the analysis is performed with 8 different Galactic Center cone angles, ranging from  $5^\circ$  to  $40^\circ$  in steps of  $5^\circ$ . For the solar search, the search is much more localized directionally, with the sun having an angular diameter of just  $0.5^\circ$ . Therefore, a single cone with half opening angle of  $5^\circ$  is used for the solar search.

In order to quantify the agreement of the observed data with the background only or some level of excess signal hypothesis, a Poisson  $\chi^2$  statistic is used which incorporates the systematic uncertainty of the background estimate using the pull method [12, 35]:

$$\chi^2(s) = \min_{\epsilon} \left[ 2 \left( E - \mathcal{O} + \mathcal{O} \ln \frac{\mathcal{O}}{E} \right) + \epsilon^2 \right] \quad (4.8)$$

where,

$$E = b(1 + \epsilon\sigma) + s \quad (4.9)$$

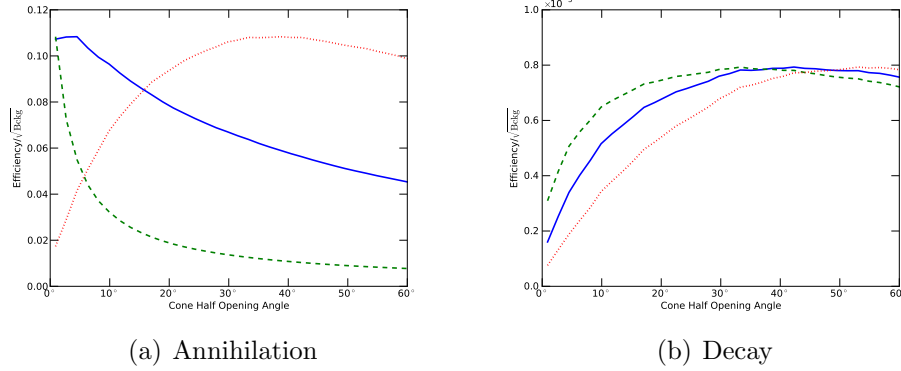


**Figure 4.8:** Cone opening angle optimization for boosted dark matter from annihilation and decay. In both 4.8(a) and 4.8(b) the solid blue is the NFW halo model, dotted red is the Kravtsov halo model, and dashed green is the Moore halo model. Note since the scaling is arbitrary, the efficiencies have been scaled by different amounts for each model so that they can all be seen on the same plot.

and  $b$  is the estimated background with systematic uncertainty  $\epsilon$ ,  $s$  is the signal excess being tested, and  $\mathcal{O}$  is the observed number of events. The test statistic  $\Delta\chi^2$  is calculated by subtracting from  $\chi^2$  for the particular value of  $s$  the minimum  $\chi^2$  for any value of  $s$ . Note that this  $\chi_{\min}^2$  is easily computed as:

$$\chi_{\min}^2 = \begin{cases} 0, & \text{if } b \leq \mathcal{O} \\ \chi^2(0), & \text{if } b > \mathcal{O} \end{cases} \quad (4.10)$$

For each tested value of  $s$ , a large number of toy MC are produced. If the fraction of toy MC produced with  $\Delta\chi^2(s)$  less than the value found for the data is greater than or equal to  $\alpha$ , then  $s$  is excluded at  $\alpha$  confidence [36].

The minimization of  $\chi^2$  over  $\epsilon$  is done by setting

$$\frac{\partial\chi^2}{\partial\epsilon} = 2(b\sigma - \frac{\mathcal{O}b\sigma}{b(1+\sigma\epsilon) + s}) + 2\epsilon = 0. \quad (4.11)$$



Equation 4.11 leads to a simple quadratic equation with solutions

$$\epsilon = \frac{-(b\sigma^2 + 1 + s/b) \pm \sqrt{(b\sigma^2 + 1 + s/b)^2 - 4\sigma(b\sigma + \sigma s - \mathcal{O}\sigma)}}{2\sigma}. \quad (4.12)$$

Both solutions to Equation 4.12 are tested, and the smaller of the two resulting  $\chi^2$  values is taken as the correct  $\chi^2$ . Note that if  $\epsilon < -1/\sigma$ , which would imply pulling the background to a negative value, then  $\epsilon$  is set to  $-1/\sigma$  so that the background is pulled to 0. Generally this would only happen for Data and MC which agree very poorly with a large systematic uncertainty, however it must be accounted for since it could occur a small number of times over many toy MC samples.

#### 4.6.1 Trials Factors

The correlations between the 8 galactic center cones (the smaller cones are subsets of the larger cones) leads to complicated trials factors when trying to understand the significance of any excess. In order to understand the trials factors, 250,000 toy mc ensembles were created for both low and medium energy samples. For each energy range, 8 bins in  $\cos\theta_{GC}$  of width  $5^\circ$  are shifted by a single shared systematic error for that energy range, chosen from a random Gaussian distribution with width given by the systematic uncertainties computed in Section 4.7. From the expected background, the number of toy mc events in each bin is then chosen as a Poisson random variable. The number of events in each of the 8 cones around the galactic center is then calculated for the toy mc ensemble by adding up the events in the bins contained in each cone. The significance of any excess in each cone is computed as described above, and the largest excess out of the 8 cones is recorded. The probability that at least 1 of the 8 cones finds an excess of a particular significance  $\alpha$  is then calculated, which allows for the adjustment of the significance to include the trials

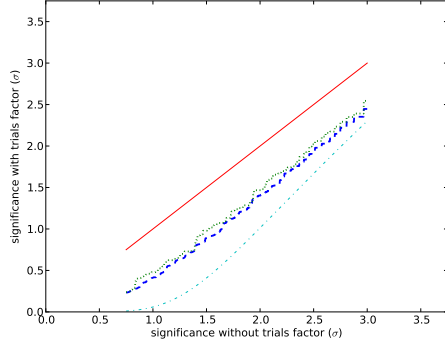


**Figure 4.9:** Trials factor effect. The dashed blue (dotted green) line converts the significance of an excess without the trials factor included into the significance with the trials factor included for the low (medium) energy sample, based on Toy MC. As reference, the solid red line shows  $y=x$ , the conversion for perfectly correlated measurements, and the dashed-dotted cyan line shows the conversion for 8 uncorrelated measurements. Note that the effect for the galactic center cones falls between the perfectly correlated and perfectly uncorrelated effects, as expected.

factor. The results of this study are shown in Figure 4.9. Note that the results fall between the expectations for 8 perfectly correlated or 8 completely uncorrelated measurements.

#### 4.6.2 Limits on a simple Model

Reference [26] presents a baseline boosted dark matter model. In this model, a heavy dark matter particle  $A$  is the dominant dark matter of the universe. This particle  $A$  does not couple directly to standard matter, but instead annihilates into a lighter dark matter particle  $B$ , which couples to standard matter through the exchange of a dark photon  $m_{\gamma'}$ , as in Figure 4.10. The relic abundance of  $A$  is determined by an assisted freeze out scenario, and the thermal cross section is set to  $\langle\sigma_{A\bar{A}\rightarrow B\bar{B}}\rangle = 5 \times 10^{-26} \text{ cm}^3/\text{s}$  in order to achieve the observed relic density  $\Omega_A \approx 0.2$  [26]. The flux

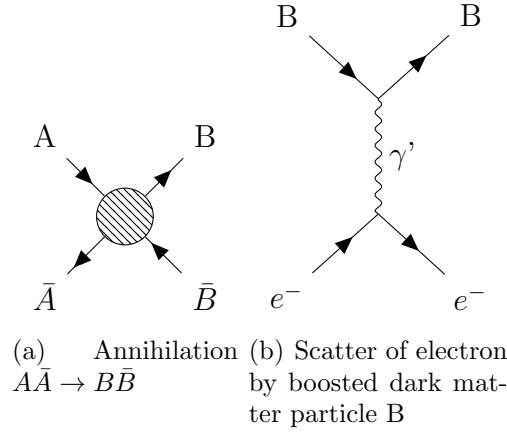


**Figure 4.10:** Feynman diagrams of boosted dark matter creation by annihilation of dominant heavy dark matter particles, and scatter of electron by boosted dark matter through exchange of a dark photon.

of boosted dark matter from the galactic center is

$$\frac{d\Phi}{d\Omega dE_B} = \frac{1}{2} \frac{r_{\text{sun}}}{4\pi} \left( \frac{\rho_{\text{local}}}{m_A} \right)^2 \mathcal{J} \langle \sigma_{A\bar{A} \rightarrow B\bar{B}} \rangle \delta(E_B - m_A). \quad (4.13)$$

Note that any adjustment to the thermal cross section simply results in a corresponding scaling of the limits on  $\sigma_{Be^- \rightarrow Be^-}$  found in Section 4.8.

This model can be described by four free parameters: The mass of the dominant dark matter species  $m_A$ , the mass of the boosted dark matter  $m_B$ , the mass of the dark photon  $m_{\gamma'}$ , and the total cross section of the boosted dark matter on electrons  $\sigma_{\text{tot}}$ . Since the boosted dark matter is coming from annihilation of A, the energy of the boosted dark matter is equal to  $m_A$ . The maximum energy of the recoil electron scattered by the boosted dark matter is then set by kinematics:

$$E_e^{\text{max}} = m_e \frac{(m_A + m_e)^2 + m_A^2 - m_B^2}{(m_A + m_e)^2 - m_A^2 + m_B^2}. \quad (4.14)$$

The shape of the recoil electron spectrum is largely set by the mass of the dark

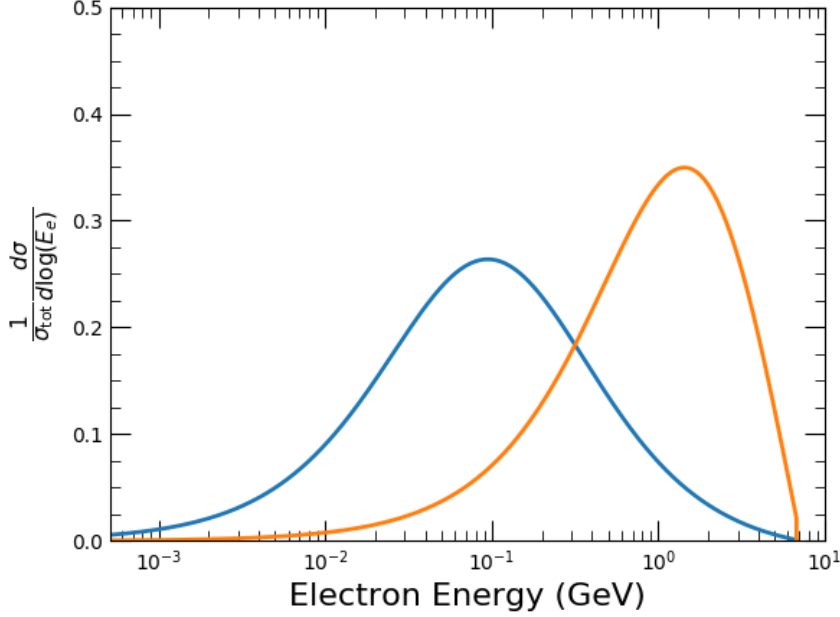


**Figure 4.11:** Recoil electron spectrum for simple model. The blue is for  $m_{\gamma'} = 10$  MeV, while the red is for  $m_{\gamma'} = 50$  MeV. Both use values of  $m_A = 20$  GeV and  $m_B = 200$  MeV.

photon, with lower values of the dark photon mass leading to a spectrum more peaked towards smaller electron recoil energies, as shown in Figure 4.11. The value  $\sigma_{\text{tot}}$  acts simply as a scaling factor.

A fit was performed over this four-dimensional parameter space. For each halo model, the number of expected signal events in each energy range at any particular point in parameter space is predicted by reweighting the signal MC discussed in Section 4.4. This reweighting accounts for the model dependent recoil electron energy spectrum, as well as the model dependent smearing between the boosted dark matter direction and the recoil electron direction. A binned  $\chi^2$  statistic was then computed similar to the one described above:

$$\chi^2(m_A, m_B, m_{\gamma'}, \sigma_{\text{tot}}) = \sum_i^3 \min_{\epsilon_i} \left[ 2 \left( E_i - \mathcal{O}_i + \mathcal{O}_i \ln \frac{\mathcal{O}_i}{E_i} \right) + \epsilon_i^2 \right] \quad (4.15)$$

where

$$E_i = b_i(1 + \epsilon_i \sigma_i) + s_i. \quad (4.16)$$

Note that there are 3 uncorrelated systematic errors representing the systematic uncertainty on the background estimate for each energy bin and no systematic uncertainty included for the signal. A minimum  $\chi^2$  over the whole 4-D parameter space was found, and the  $\Delta\chi^2$  test statistic was defined as

$$\Delta\chi^2(m_A, m_B, m_{\gamma'}, \sigma_{\text{tot}}) = \chi^2(m_A, m_B, m_{\gamma'}, \sigma_{\text{tot}}) - \chi_{\text{min}}^2. \quad (4.17)$$

Note that the  $\chi_{\text{min}}^2$  used here is different from the one found in Equation (4.10). Additionally, each halo model was considered separately so that there was a different minimum used for the Moore, NFW, and Kravtsov models, respectively. For each halo model only a single search cone was considered, with the  $5^\circ$  cone chosen for the Moore halo, the  $10^\circ$  cone chosen for the NFW model, and the  $40^\circ$  cone chosen for the Kravtsov model. The choice of search cone for each model was made based on Figure 4.8. Frequentist confidence regions could then be defined using toy MC. A point in parameter space is considered excluded at confidence level  $\alpha$  if less than  $(1-\alpha)$  of toy MC ensembles produced at the point resulted in a  $\Delta\chi^2$  at the point greater than or equal to the value found from the data. In these toy MC samples both statistical fluctuations and systematic fluctuations of the background were taken into account.

In Section 4.8, confidence regions are presented for a baseline value of  $m_{\gamma'} = 20$  MeV in the plane  $\sigma_{\text{tot}}/m_A^2$  vs  $E_{\text{max}}$  where  $E_{\text{max}}$  has been defined in Equation (4.14). The 4-D space  $(m_A, m_B, m_{\gamma'}, \sigma_{\text{tot}})$  is thus profiled down to a 3-D space  $(E_{\text{max}}, m_{\gamma'}, \sigma_{\text{tot}}/m_A^2)$ . Since the boosted dark matter flux goes as  $1/m_A^2$  (See Equation (4.13)),  $\sigma_{\text{tot}}/m_A^2$  is

proportional to the total signal event rate, and so all points in 4-D parameter space which are profiled onto the same point in 3-D parameter space will have very similar expected numbers of signal events.

The computation of confidence regions in the profiled space is performed as follows [12]. First, the set  $U_{E_{\max}, \sigma_{\text{tot}}/m_A^2}$  is defined as the set of all values of  $(m_A, m_B, \sigma_{\text{tot}})$  which correspond to  $E_{\max}$  and  $\sigma_{\text{tot}}/m_A^2$ . Then the profile  $\hat{\chi}^2$  and profile  $\Delta\hat{\chi}^2$  are defined as:

$$\hat{\chi}^2(E_{\max}, m_{\gamma'}, \sigma_{\text{tot}}/m_A^2) = \min_{(m_A, m_B, \sigma_{\text{tot}}) \in U_{E_{\max}, \sigma_{\text{tot}}/m_A^2}} \chi^2(m_A, m_B, m_{\gamma'}, \sigma_{\text{tot}}) \quad (4.18)$$

$$\Delta\hat{\chi}^2(E_{\max}, m_{\gamma'}, \sigma_{\text{tot}}/m_A^2) = \hat{\chi}^2(E_{\max}, m_{\gamma'}, \sigma_{\text{tot}}/m_A^2) - \chi_{\min}^2. \quad (4.19)$$

A point  $(E_{\max}, m_{\gamma'}, \sigma_{\text{tot}}/m_A^2)$  is considered excluded at confidence level  $\alpha$  if there is no point in  $U_{E_{\max}, \sigma_{\text{tot}}/m_A^2}$  with the given value of  $m_{\gamma'}$  for which more than or equal to  $(1-\alpha)$  of toy MC ensembles produced at the point result in a  $\Delta\hat{\chi}^2$  greater than or equal to the one found in the data.

## 4.7 Background Estimation

In order to estimate the expected background in the Low Energy and Mid Energy samples, a data based technique was used which minimizes the effect of any systematic uncertainties on the background estimate. For a detector operated uniformly over a long period of time, different right ascensions at the same declination will all correspond to the same set of directions in detector coordinates. This means that the expected background in a cone around the galactic center can be estimated by counting all events in the same declination band as the cone. In order to avoid contaminating the background estimate with a potential signal excess from the search

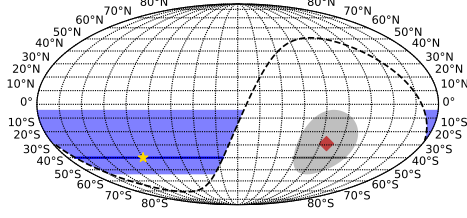


**Figure 4.12:** “Away From Source” (AFS) region shown in blue, and search cone shown in gray for a search cone of  $25^\circ$  half-opening angle around the galactic center. The red diamond is at the location of the galactic center. The dotted black line represents the  $80^\circ$  cone outside of which the AFS region is defined. For an event at the location of the yellow star, the weight for background estimation is the ratio of the gray arc to the blue arc.

cone, only events with  $\theta_{GC} > 80^\circ$  are included in the background estimate. The background estimate “Away From Source” (AFS) region and search cone are shown for a  $25^\circ$  degree cone around the Galactic Center in Figure 4.12.

Since at the same declination the AFS region and search cone span different amounts of right ascension, events found in the AFS region must be weighted according to their declination in order to find the correct background estimate for the search cone. The weight of each event in the AFS region is equal to the ratio of right ascensions spanned by the search cone to right ascensions spanned by the AFS region at that declination, which is visualized in Figures 4.12 and 4.13(a). This weight can be written in terms of the variables in Figure 4.13(b) as  $w = \frac{\alpha_{\text{cone}}}{\pi - \alpha_{\text{AFS}}}$ . To compute  $\alpha_{\text{cone}}$  and  $\alpha_{\text{AFS}}$ , the points must be found where a cone of half opening angle  $\theta$  centered on the direction to the galactic center, a plane at declination  $\phi_{\text{dec}}$ , and the unit sphere intersect. (The directions are without loss of generality assumed to be unit vectors, thus the inclusion of the unit sphere requirement). In Figure 4.13(a), for the AFS region (GC search cone), these points are at the intersection of the blue (gray)

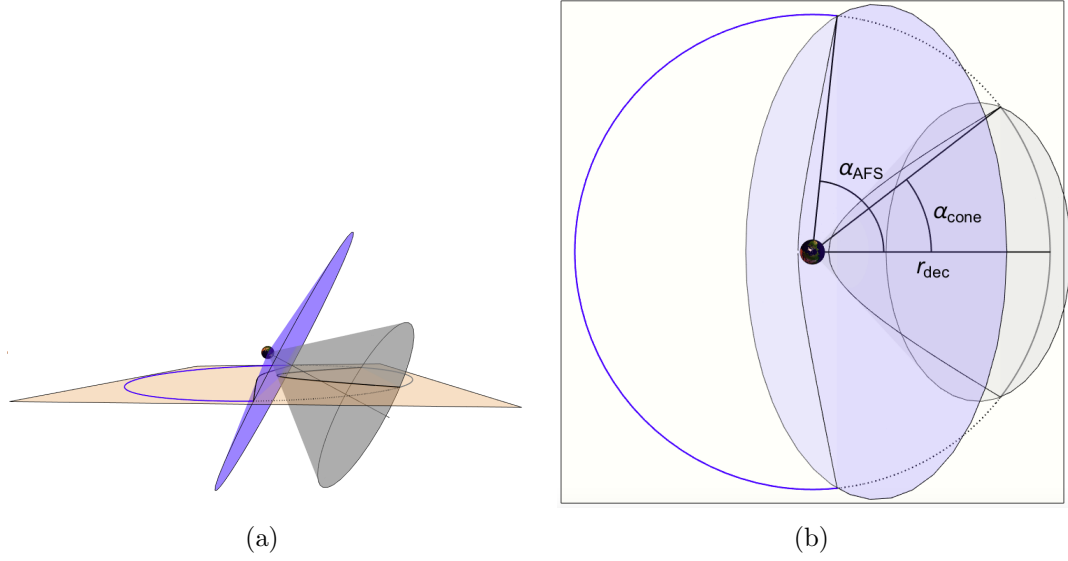


**Figure 4.13:** Visualization of the event weighting for background estimation. An event found in the AFS region at the declination represented by the plane is weighted by the ratio of the gray arc to the blue arc. Figure 4.13(b) shows Figure 4.13(a) as seen from directly above. The Mathematica code used to create these images can be found in ??

cone, pink plane, and the circle drawn on the plane. The circle in Figure 4.13(b) is the intersection of the plane and the unit sphere, and so  $r_{\text{dec}} = \cos \phi_{\text{dec}}$ . Defining the x-axis as pointing toward the right ascension of the galactic center at declination 0, the z-axis as extending from the poles of the earth so that  $+\hat{z}$  corresponds with a declination of  $90^\circ$  and  $-\hat{z}$  with a declination of  $-90^\circ$ , and the y-axis accordingly to keep the coordinate system right handed, we can write the position of the two intersection points as:

$$\hat{v}_{\pm} = (x', \pm y', z') \quad (4.20)$$

and the Galactic Center direction as:

$$\hat{v}_{\text{GC}} = (\cos(-29^\circ), 0, \sin(-29^\circ)) \quad (4.21)$$



Since  $\hat{v}_\pm$  are on the plane at declination  $\phi_{\text{dec}}$  we have:

$$z' = \sin \phi_{\text{dec}} \quad (4.22)$$

Additionally, since  $\hat{v}_\pm$  are on the cone of half opening angle  $\theta$  around the Galactic Center we have

$$\frac{|\hat{v}_\pm - (\hat{v}_\pm \cdot \hat{v}_{\text{GC}}) \hat{v}_{\text{GC}}|}{|(\hat{v}_\pm \cdot \hat{v}_{\text{GC}}) \hat{v}_{\text{GC}}|} = \tan \theta \quad (4.23)$$

$$\hat{v}_\pm \cdot \hat{v}_{\text{GC}} > 0 \quad (4.24)$$

Solving Equation 4.23 under the condition of Equation 4.24, we have:

$$\frac{\sqrt{(\hat{v}_\pm - (\hat{v}_\pm \cdot \hat{v}_{\text{GC}}) \hat{v}_{\text{GC}}) \cdot (\hat{v}_\pm - (\hat{v}_\pm \cdot \hat{v}_{\text{GC}}) \hat{v}_{\text{GC}})}}{\sqrt{((\hat{v}_\pm \cdot \hat{v}_{\text{GC}}) \hat{v}_{\text{GC}}) \cdot ((\hat{v}_\pm \cdot \hat{v}_{\text{GC}}) \hat{v}_{\text{GC}})}} = \tan \theta \quad (4.25)$$

$$\frac{\sqrt{\hat{v}_\pm \cdot \hat{v}_\pm + (\hat{v}_{\text{GC}} \cdot \hat{v}_{\text{GC}} - 2)(\hat{v}_\pm \cdot \hat{v}_{\text{GC}})^2}}{\sqrt{(\hat{v}_\pm \cdot \hat{v}_{\text{GC}})^2 \hat{v}_{\text{GC}} \cdot \hat{v}_{\text{GC}}}} = \tan \theta \quad (4.26)$$

$$\frac{\sqrt{1 - (\hat{v}_\pm \cdot \hat{v}_{\text{GC}})^2}}{\hat{v}_\pm \cdot \hat{v}_{\text{GC}}} = \tan \theta \quad (4.27)$$

$$1 - (\hat{v}_\pm \cdot \hat{v}_{\text{GC}})^2 = \tan^2 \theta (\hat{v}_\pm \cdot \hat{v}_{\text{GC}})^2 \quad (4.28)$$

$$\hat{v}_\pm \cdot \hat{v}_{\text{GC}} = \sqrt{\frac{1}{1 + \tan^2 \theta}} \quad (4.29)$$

$$x' \cos(-29^\circ) + \sin \phi_{\text{dec}} \sin(-29^\circ) = \sqrt{\frac{1}{1 + \tan^2 \theta}} \quad (4.30)$$

$$x' = \frac{-\sin \phi_{\text{dec}} \sin(-29^\circ) + \sqrt{\frac{1}{1 + \tan^2 \theta}}}{\cos(-29^\circ)} \quad (4.31)$$

where we have used the fact that  $(\hat{v}_{\text{GC}} \cdot \hat{v}_{\text{GC}}) = (\hat{v}_\pm \cdot \hat{v}_\pm) = 1$ . The angle  $\alpha$  is then found as

$$\cos \alpha = \frac{x'}{r_{\text{dec}}} = \frac{-\sin \phi_{\text{dec}} \sin(-29^\circ) + \sqrt{\frac{1}{1 + \tan^2 \theta}}}{\cos(-29^\circ) \cos \phi_{\text{dec}}} \quad (4.32)$$

The weight for an event in the AFS region at declination  $\phi_{\text{dec}}$  can thus be found as

$$w(\phi_{\text{dec}}) = \frac{\alpha_{\text{cone}}}{\pi - \alpha_{\text{AFS}}} \quad (4.33)$$

$$\cos \alpha_{\text{cone}} = \frac{-\sin \phi_{\text{dec}} \sin(-29^\circ) + \sqrt{\frac{1}{1 + \tan^2 \theta_{\text{cone}}}}}{\cos(-29^\circ) \cos \phi_{\text{dec}}} \quad (4.34)$$

$$\cos \alpha_{\text{AFS}} = \frac{-\sin \phi_{\text{dec}} \sin(-29^\circ) + \sqrt{\frac{1}{1 + \tan^2 \theta_{\text{AFS}}}}}{\cos(-29^\circ) \cos \phi_{\text{dec}}} \quad (4.35)$$

The background estimate and uncertainty on the estimate are then

$$B_{\text{est}} = \sum_i w(\phi_{\text{dec},i}) \quad (4.36)$$

$$\sigma B_{\text{est}} = \sqrt{\sum_i w^2(\phi_{\text{dec},i})}. \quad (4.37)$$

A similar technique could be applied to the search around the sun, however the declination of the sun changes with time, and so the math becomes more complicated. Instead, a slightly different approach was taken. The search cone for the solar search is a  $5^\circ$  cone around the sun, and everything outside of this cone is taken as the AFS region. For an event in the AFS region, the correct weight to use for background estimation is then the ratio of time that the horizontal coordinate direction of the event is within the  $5^\circ$  cone around the sun to the time it is outside the cone. These weights are calculated as follows. Direction in horizontal coordinates are divided into a grid of 1000 bins in azimuth by 600 bins in cosine zenith. The weight for events in each bin is then computed by stepping through a year in steps of 1 second and counting up the amount of time each bin is within  $5^\circ$  of the sun. The fraction of time spent within  $5^\circ$  of the sun as a function of cosine zenith and azimuth is shown in Figure 4.14

In both the application to the galactic center and to the sun it is implicitly assumed

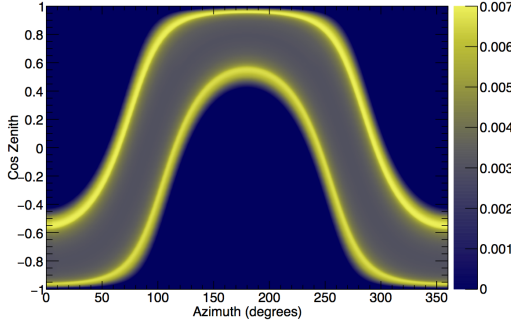


**Figure 4.14:** The fraction of time spent with  $5^\circ$  of the sun, as a function of cosine zenith and azimuth.

that the detector has been run uniformly in time. This assumption could introduce error in the background estimates if instead the detector has run much more at certain times of the day or year than at others. Therefore 500 years of atmospheric neutrino MC was used to test the validity of the AFS method. The time of each MC event was chosen from the times of real data events. The AFS method was applied to the MC. The background estimate made by the AFS method applied to the MC was compared to the number of events found in the search cone in the MC. If these numbers were found to be very different, it would indicate non-uniformity of the time when the detector has been run is leading to a bias in the AFS background estimate. As can be seen in Figure 4.15, the difference is both statistically consistent with 0, and much smaller than the uncertainty in the AFS background estimates when applied to real data. Therefore, any potential bias in the AFS method introduced by non-uniform running of the detector can be ignored.

For the High Energy event sample, there would be too few events in the AFS region for the above technique to work well. Instead, the MC estimate for the expected number of atmospheric neutrino events in the search cone was taken as the background estimate. The MC was livetime normalized and oscillated according to 3-flavor oscillations with oscillation parameters  $\Delta M_{23}^2 = 2.5 \times 10^{-3} \text{ GeV}^2$ ,  $\Delta M_{12}^2 = 7.65 \times 10^{-5}$

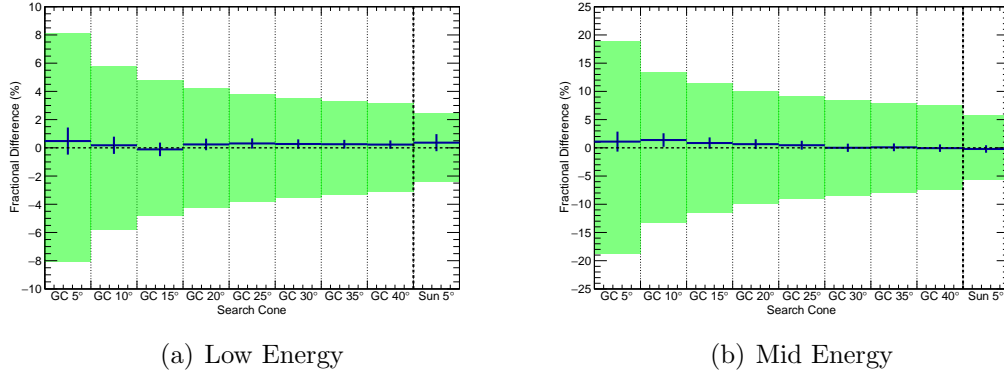


**Figure 4.15:** Verification of AFS method. The blue histogram shows the fractional difference between the AFS background estimate when applied to MC and the actual number of events in the search cone in MC. The green shows the AFS background estimate uncertainty when applied to data.

GeV<sup>2</sup>,  $\sin^2 \theta_{23} = 0.5875$ ,  $\sin^2 \theta_{13} = 0.0219$ ,  $\sin^2 \theta_{12} = 0.309$ ,  $\delta_{cp} = 4.19$ . The systematic uncertainty on this estimate is found by summing in quadrature the effect of and 1- $\sigma$  shift of all 75 official SK-IV systematics. The uncertainty of oscillation parameters were also included as systematics. Of these only 18 cause more than a 1% shift in our background estimate at 1- $\sigma$ . The uncertainties which cause more than a 5% shift at 1- $\sigma$  are shown in Table 4.3. As seen in Table 4.3, the systematic uncertainty of the Higher Energy sample is dominated by the systematic uncertainty of the neutron tagging cut. This uncertainty accounts for the uncertainty in the efficiency of our neutron tagging algorithm, as well as the uncertainty in the production and transport of neutrons in the detector. It was estimated by a Data-MC comparison of the fraction of events passing the first three selection cuts which also had zero tagged neutrons as a function of visible energy. Above about 10 GeV of visible energy, there are very low statistics for the data, and so a Data-MC comparison is difficult to make. Therefore, above 3 GeV both the data and MC were fitted to logarithmic functions  $A + B \log \frac{E_{vis}}{\text{GeV}}$ , as shown in Figure 4.16(a). The systematic uncertainty was then taken

as the difference between the Data fit and the MC fit in the region above 7.6 GeV of visible energy. The total uncertainty for the High Energy event sample is 29.8%.

The background estimate results for the 8 cone sizes around the galactic center and the  $5^\circ$  cone around the Sun are shown in Table 4.4. The background estimates for the low and mid energy regions are compared to MC background estimates in Figure 4.17. The systematic uncertainties on the MC background estimates for the low and mid energy samples were computed in the same way as for the high energy sample, resulting in uncertainties of 18.4% and 17.7% respectively. As can be seen in Figure 4.17, the two background estimation techniques agree with one another to within systematic uncertainties, and the systematic uncertainties on the AFS technique are much smaller than those on the MC based estimate.

Systematic	1- $\sigma$ shift
Neutron Tagging Cut	23%
Normalization (Flux, Data reduction, FV)	11%
Energy Calibration	6%
Garczyk and Soczyk $1\pi$ axial coupling	5%

**Table 4.3:** Largest systematic uncertainty contributions for High Energy sample.

## 4.8 Results

The galactic center and solar searches were performed on 2628.1 days of SK-IV data, which corresponds to 161.9 kton-years. The results of the searches are summarized in Tables 4.5 to 4.7. There are no indications of excesses from the galactic center or the sun. The results are converted to event rate limits and presented in Figure 4.18. The locations of all events in the sky are shown in Figures 4.19 and 4.20. As can be seen there is no visual clustering of events around the galactic center.

Limits were also calculated on a simple model, as described in Section 4.6.2. Since

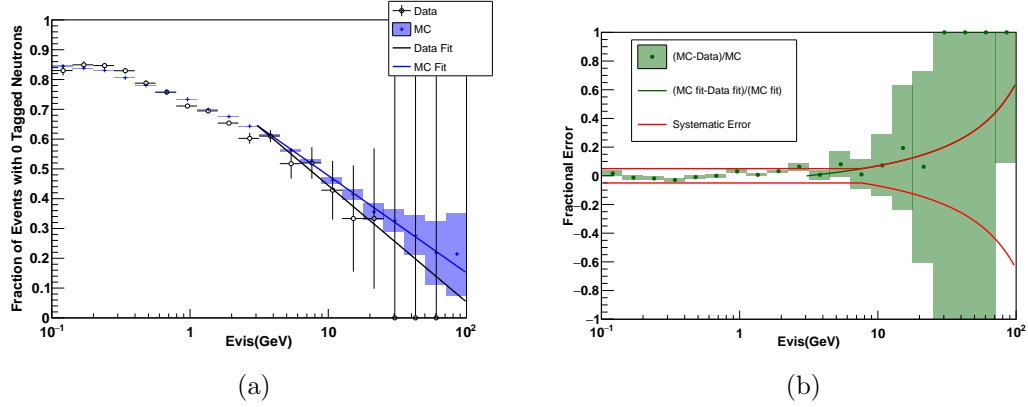


**Figure 4.16:** Neutron tagging cut systematic error estimation. 4.16(a) shows the fractional number of events passing the neutron tagging cut after passing all previous cuts for both Data and MC, along with logarithmic fits. The filled rectangles around the MC show statistical uncertainty in the MC. 4.16(b) shows the resulting systematic uncertainty, set to 5% below 7.6 GeV, and the difference in the two fits from 4.16(a) above 7.6 GeV.

the point with  $\sigma_{\text{tot}}$  is allowed at 90% CI, the 90% CI contours can be interpreted as 90% CI upper limits. These upper limits are presented for  $m_{\gamma'} = 20\text{MeV}$  in Figure 4.21. When  $E_{\text{max}} > 10\text{ GeV}$ , the effect of the detector energy threshold is negligible, and the 90% CI upper limit on  $\sigma_{\text{tot}}/m_A^2$  remains constant as  $E_{\text{max}}$  increases. In this region the limit for  $m_{\gamma'} = 20\text{MeV}$  with the NFW halo model is found to be  $1.5 \times 10^{-37}(\text{cm}^2/\text{GeV}^2)$ .

## 4.9 Conclusion

A search for an excess of electron-elastic-scatter-like events from the galactic center or the sun was performed over 2628.1 days of SK-IV data, which corresponds to 161.9 kton-years. No excess above atmospheric neutrino background was observed around with the galactic center of the sun. Limits were computed for a simple boosted dark matter model which would be expected to produce such events in SK, and in

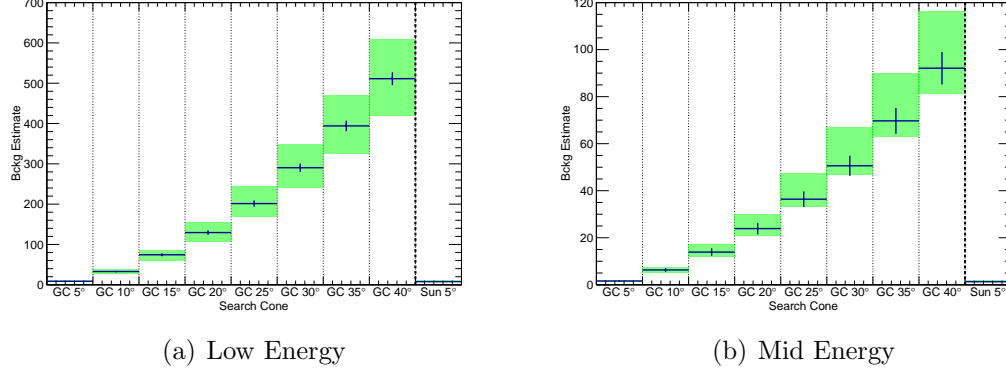


**Figure 4.17:** Comparison of AFS background estimates to MC background estimates for Low Energy and Mid Energy samples. The two background estimation techniques agree to within systematic uncertainties, and the AFS technique has much smaller systematic uncertainties.

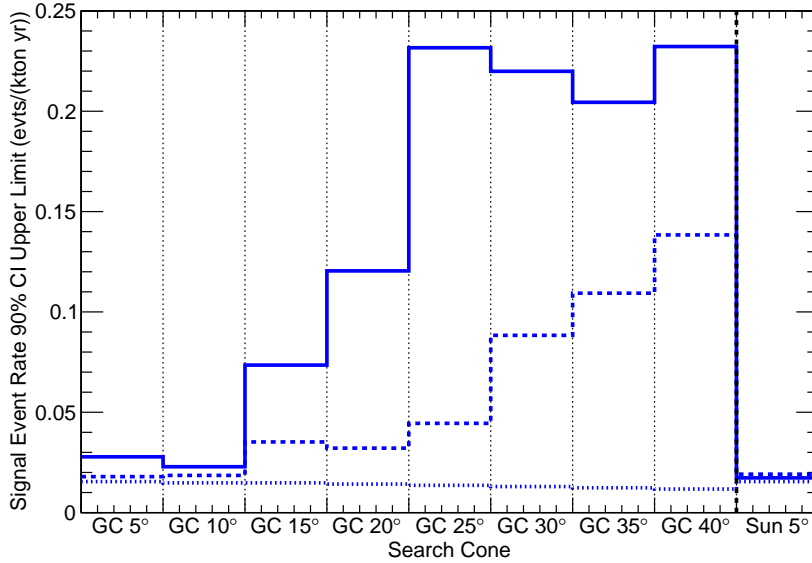


**Figure 4.18:** Signal event rate 90% C.I. upper limits for SubGeV (solid line), Mid Energy (dashed line), and High Energy (dotted line) samples.

	Low Energy	Mid Energy	High Energy
GC 5° cone	$8.6 \pm 0.7$	$1.6 \pm 0.3$	$0.011 \pm 0.003$
GC 10° cone	$32.9 \pm 1.9$	$6.3 \pm 0.84$	$0.041 \pm 0.012$
GC 15° cone	$74.4 \pm 3.6$	$13.9 \pm 1.6$	$0.096 \pm 0.029$
GC 20° cone	$129.9 \pm 5.5$	$23.9 \pm 2.4$	$0.17 \pm 0.05$
GC 25° cone	$201.4 \pm 7.7$	$36.4 \pm 3.3$	$0.26 \pm 0.08$
GC 30° cone	$290.3 \pm 10.2$	$50.6 \pm 4.3$	$0.37 \pm 0.11$
GC 35° cone	$394.1 \pm 13.0$	$69.7 \pm 5.5$	$0.49 \pm 0.15$
GC 40° cone	$511.2 \pm 16.0$	$92.1 \pm 6.9$	$0.63 \pm 0.19$
Sun 5° cone	$7.74 \pm 0.19$	$1.29 \pm 0.08$	$0.011 \pm 0.003$

**Table 4.4:** Background estimates for the three energy ranges for 8 cone sizes around the galactic center and a 5° cone around the sun. Uncertainties on the background estimates are the systematic uncertainties as discussed in the text.

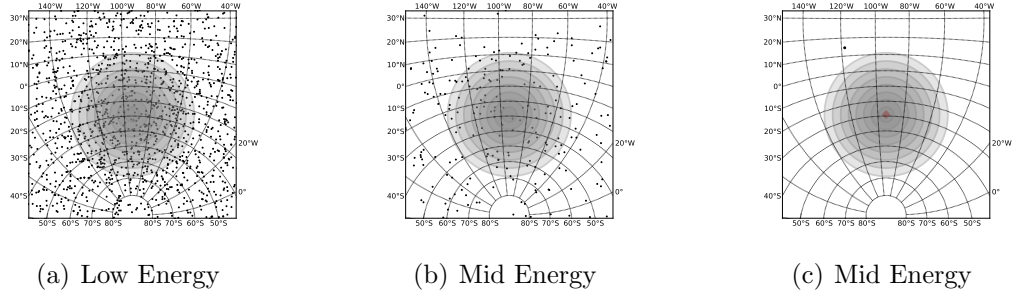


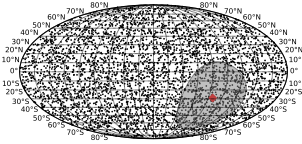
**Figure 4.19:** Location of all events passing analysis cuts near the galactic center. The 8 grey circles show the 8 cones around the galactic center used in the analysis.

the region of  $E_{\text{max}} > 10\text{GeV}$ , the 90% CI upper limit on  $\sigma_{\text{tot}}/m_A^2$  was found to be  $1.5 \times 10^{-37} \text{ (cm}^2/\text{GeV}^2\text{)}$  for  $m_{\gamma'} = 20 \text{ MeV}$  and the NFW galactic halo model.

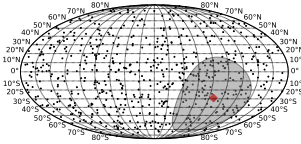


	Expected Bckg	Data	Signal 90% C.I.
GC 5° cone	$8.6 \pm 0.7$	7	0-4.5
GC 10° cone	$32.9 \pm 1.9$	24	0-3.7
GC 15° cone	$74.4 \pm 3.6$	70	0-11.9
GC 20° cone	$129.5 \pm 5.5$	127	0-19.5
GC 25° cone	$201.4 \pm 7.7$	211	0-37.5
GC 30° cone	$290.3 \pm 10.2$	292	0-35.6
GC 35° cone	$394.1 \pm 13.0$	387	0-33.1
GC 40° cone	$511.2 \pm 16.0$	502	0-37.6
Sun 5° cone	$7.74 \pm 0.19$	5	0-2.8

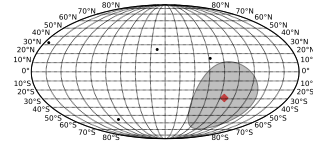
**Table 4.5:** Results for low energy events



(a) Low Energy



(b) Mid Energy



(c) Mid Energy

**Figure 4.20:** Location of all events passing analysis cuts. The grey shows a 40° cone around the galactic center, which is shown by the red diamond

	Expected Bckg	Data	Signal 90% C.I.
GC 5° cone	$1.6 \pm 0.3$	1	0-2.9
GC 10° cone	$6.3 \pm 0.84$	4	0-3.0
GC 15° cone	$13.9 \pm 1.6$	12	0-5.7
GC 20° cone	$23.9 \pm 2.4$	19	0-5.2
GC 25° cone	$36.4 \pm 3.3$	31	0-7.2
GC 30° cone	$50.6 \pm 4.3$	50	0-14.3
GC 35° cone	$69.7 \pm 5.5$	70	0-17.7
GC 40° cone	$92.1 \pm 6.9$	94	0-22.4
Sun 5° cone	$1.29 \pm 0.08$	1	0-3.1

**Table 4.6:** Results for medium energy events

	Expected Bckg	Data	Signal 90% C.I.
GC 5° cone	$0.011 \pm 0.003$	0	0-2.5
GC 10° cone	$0.041 \pm 0.012$	0	0-2.4
GC 15° cone	$0.096 \pm 0.029$	0	0-2.4
GC 20° cone	$0.17 \pm 0.05$	0	0-2.3
GC 25° cone	$0.26 \pm 0.08$	0	0-2.2
GC 30° cone	$0.37 \pm 0.11$	0	0-2.1
GC 35° cone	$0.49 \pm 0.15$	0	0-2.0
GC 40° cone	$0.63 \pm 0.19$	0	0-1.9
Sun 5°	$0.011 \pm 0.003$	0	0-2.5

**Table 4.7:** Results for high energy events

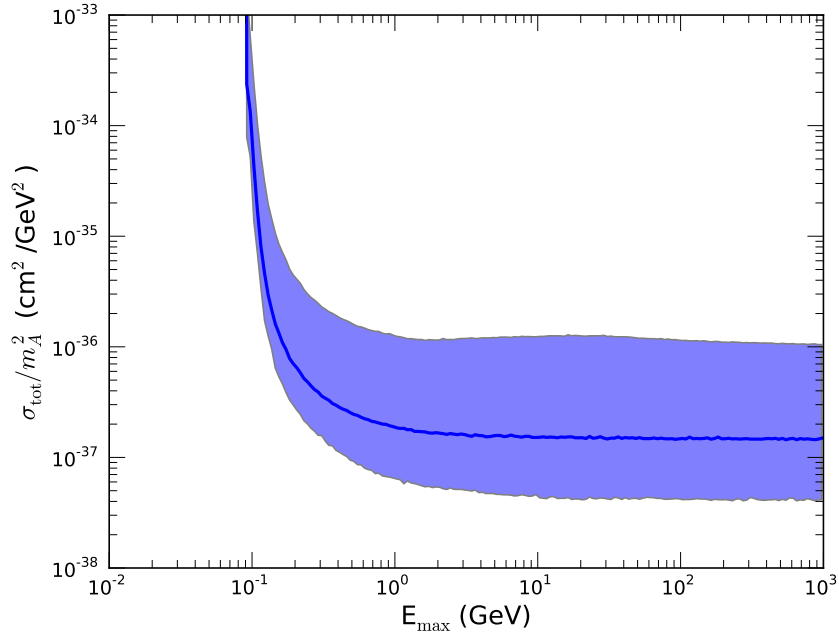


**Figure 4.21:** Limits on simple model, for  $m_{\gamma'} = 20$  MeV. The dark blue line is for the NFW halo, and the upper and lower limits of the band are for the Kravtsov and Moore models, respectively.

# Bibliography

- [1] H. Yüksel, *et al.* Physical Review D **76**, 12 123506 (2007)
- [2] P. A. R. Ade, *et al.* Astron. Astrophys. **594** A13 (2016)
- [3] G. Hinshaw, *et al.* Astrophys. J. Suppl. **208** 19 (2013)
- [4] L. M. Brown. Phys. Today **31N9** 23 (1978)
- [5] E. Fermi. Z. Phys. **88** 161 (1934)
- [6] F. Reines, C. L. Cowan. Phys. Rev. **92** 830 (1953)
- [7] C. L. Cowan, *et al.* Science **124** 103 (1956)
- [8] F. Reines, C. L. Cowan. Nature **178** 446 (1956)
- [9] Y. Fukuda, *et al.* Nucl. Instrum. Meth. **A501** 418 (2003)
- [10] K. Abe, *et al.* Nucl. Instrum. Meth. **A737** 253 (2014)
- [11] J. D. Jackson. *Classical Electrodynamics*. Wiley (1998)
- [12] C. Patrignani, *et al.* Chin. Phys. **C40**, 10 100001 (2016)
- [13] F. Zwicky. Helv. Phys. Acta **6** 110 (1933). [Gen. Rel. Grav.41,207(2009)]

- [14] V. C. Rubin, N. Thonnard, W. K. J. Ford. The Astrophysical Journal **238** 471 (1980)
- [15] K. G. Begeman, A. H. Broeils, R. H. Sanders. Mon. Not. Roy. Astron. Soc. **249** 523 (1991)
- [16] G. R. Blumenthal, *et al.* Nature **311**, 5986 517 (1984)
- [17] L. Collaboration, *et al.* arXiv.org (2013)
- [18] The CDMS II Collaboration. Science **327**, 5973 1619 (2010)
- [19] E. Aprile, *et al.* Physical Review Letters **109**, 18 181301 (2012)
- [20] S. Desai, *et al.* Phys. Rev. **D70** 083523 (2004). [Erratum: Phys. Rev.D70,109901(2004)]
- [21] M. Rameez, T. Montaruli. PoS **ICRC2015** 1209 (2016)
- [22] S. Adrian-Martinez, *et al.* JCAP **1311** 032 (2013)
- [23] V. Khachatryan, *et al.* Eur. Phys. J. **C75**, 5 235 (2015)
- [24] G. Aad, *et al.* Eur. Phys. J. **C75**, 7 299 (2015). [Erratum: Eur. Phys. J.C75,no.9,408(2015)]
- [25] J. Goodman, *et al.* Phys. Rev. **D82** 116010 (2010)
- [26] K. Agashe, *et al.* JCAP **1410**, 10 062 (2014)
- [27] J. F. Cherry, M. T. Frandsen, I. M. Shoemaker. Physical Review Letters **114**, 23 231303 (2015)
- [28] A. Bhattacharya, R. Gandhi, A. Gupta. JCAP **1503**, 03 027 (2015)

- [29] J. Kopp, J. Liu, X.-P. Wang. Journal of High Energy Physics **2015**, 4 105 (2015)
- [30] K. Kong, G. Mohlabeng, J.-C. Park. Physics Letters B **743**, C 256 (2015)
- [31] J. Berger, Y. Cui, Y. Zhao. Journal of Cosmology and Astroparticle Physics **2014**, 10 062 (2014)
- [32] J. F. Navarro, C. S. Frenk, S. D. M. White. The Astrophysical Journal **462** 563 (1996)
- [33] B. Moore, *et al.* Monthly Notices of the Royal Astronomical Society **310**, 4 1147 (1999)
- [34] A. V. Kravtsov, *et al.* The Astrophysical Journal **502**, 1 48 (1998)
- [35] G. L. Fogli, *et al.* Physical Review D **66**, 5 053010 (2002)
- [36] G. J. Feldman, R. D. Cousins. Physical Review D **57**, 7 3873 (1998)

# Curriculum Vitae

## Christopher J. Kachulis

590 Commonwealth Avenue  
Department of Physics, Boston University  
Boston, MA 02215, U.S.A.

**Mobile:** (218)461-9178  
**Office:** (617)353-6040  
**E-mail:** kachulis@bu.edu

### EDUCATION

- Boston University, Boston, Massachusetts
  - **PhD** in Experimental Particle Physics, expected in May 2018
- Yale University, New Haven, Connecticut
  - **Bachelor of Science** in Physics, June 2011

### RESEARCH EXPERIENCE

- Super-Kamiokande
  - Hardware:
    - \* Bla Bla Bla
  - Software:
    - \* you know, stuff
- MiniCLEAN
  - Hardware:
    - \* Something something
    - \* Something else
  - Software:
    - \* etc etc etc

### TEACHING EXPERIENCE

- Boston University
  - Discussion session teaching assistant for physics, Fall 2011
- Yale

– Tutoring

## PRESENTATIONS

- **Something about Leff**  
Michael Litos  
*APS April Meeting, Parallel Talk*  
St. Louis, MO, April 2008

## SELECTED PUBLICATIONS

- **Leff thing**  
D. Gastler *et al.*  
*In progress*

## OTHER PUBLICATIONS

- **PSD thing**  
W.H. Lippincott *et al.*

## REFERENCES

- Prof. Edward Kearns  
Boston University  
Department of Physics  
590 Commonwealth Avenue  
Boston, MA 02215  
Office Phone: (617)353-3425  
E-mail: kearns@bu.edu